

Numerical simulation of violent bubble motion

Wang Qian Xi^{a)}

DSO National Laboratories, 20 Science Park Drive Singapore, Singapore 118230, Republic of Singapore

(Received 5 August 2003; accepted 20 February 2004; published online 6 April 2004)

A robust mixed-Eulerian-Lagrangian modeling is presented for the simulation of violent bubble motion, which is characterized by implementing a hybrid surface interpolation for calculating the material velocity. A linear averaging approximation is deployed for the parts of the surface where the change of the surface normal within the element size is not small, and a polynomial scheme coupled with the weighted moving least squares method for the rest of the surface. Solid angles on the free surface (an open surface) are computed analytically in a closed form using the spherical triangle theory. The algorithm is validated against an experiment and an axisymmetric bubble code. Numerical analyses are carried out for the evolution of a gas bubble near an inclined rigid wall and the interaction of two gas bubbles and a free surface. The robustness of the algorithm is demonstrated through simulating sharp bubble jets, a bubble collapsing nearby a rigid wall with a large part of the bubble surface flattened against the wall, and bubbles collapsing in very close to a free surface producing sharp free surface spikes. © 2004 American Institute of Physics.
[DOI: 10.1063/1.1704645]

I. INTRODUCTION

Bubble dynamics has significant applications in studying the damages caused to hydraulic machineries by cavitation bubbles as well as the damages inflicted on marine vessels by underwater explosion bubbles. It has long been an important research field ever since the beginning of last century. Up to date, the most successful numerical modeling of bubble dynamics has been based on the boundary integral spatial solution coupled with the time integration, i.e., the mixed-Eulerian-Lagrangian method (MEL). Axisymmetric MEL was implemented for the motion of a bubble near a rigid wall by Guerri, Lucca, and Prosperetti,¹ Blake *et al.*,² Baker *et al.*,³ Best and Kucera,⁴ Zhang and Duncan,⁵ Yuan and Prosperetti,⁶ Brujan *et al.*,⁷ DeBisschop,⁸ etc. It was also deployed to simulate the interaction of a bubble with a nearby free surface by Blake and Gibson,⁹ Blake *et al.*,^{10,11} Wang *et al.*^{12,13}

Three-dimensional MEL was implemented for the motion of a bubble near an inclined wall or a structure by Chahine and Perdue,¹⁴ Chahine,¹⁵ Wilkerson,¹⁶ Harris,^{17,18} Chen *et al.*,¹⁹ and Blake *et al.*^{11,20} Zhang *et al.*²¹ simulated the interaction of two cavitation bubbles and a free surface. General reviews on bubble dynamics may be found in Plesset and Prosperetti,²² Blake and Gibson,²³ and Blake *et al.*¹¹

The essential difference among the above three dimensional algorithms lies mainly on the calculation of the material velocity on the discretized surface. Wilkerson¹⁶ and Harris^{17,18} used linear averaging approximations on the surface elements, which suffered from the nonconvergence problem under the mesh refinement (cf. Blake *et al.*²⁰). Cha-

hine and Perdue,¹⁴ Chahine¹⁵ interpolated the surface locally using quadratic polynomials, but their method fails for certain types of geometry such as a sphere.²⁰ Blake *et al.*^{11,20} interpolated the surface locally using radial basis functions. Zhang *et al.*²¹ carried the local interpolation using a nine-noded Lagrangian local interpolation. Generally, a higher order local interpolation is more accurate than a linear one when the local surface within the mesh size is close to its tangential plane. But, the surface normal may change significantly within mesh size near the bases and fronts of a sharp bubble jet and a sharp free surface spike. At those positions, the higher order local interpolation is worse than a linear one, and may provide wrong results as well as cause numerical instabilities.

A hybrid surface interpolation is implemented in this paper to compute the material velocity of the bubble and free surfaces. In which, a polynomial scheme coupled with the moving least squares method is deployed on the part of the surface where the change of the surface normal within the element size is small. A linear averaging approximation is deployed for the part of the surface where the change of the surface normal within the element size is not small, such as the bases and fronts of the bubble jet and free surface spike. This hybrid interpolation has the obvious advantages in retaining the accuracy as well as avoiding the numerical instabilities.

An important issue in the boundary integral modeling is the calculation of solid angles on the discretized surface. For a closed surface, such as a bubble surface, solid angles are available as a subset of the influence coefficients. But, the calculation of the solid angles for an open surface are a tedious task. We noticed here that solid angles could be computed analytically in a closed form using the spherical triangle theory.

The rest of the paper is organized as follows: The math-

^{a)}Present address: Maritime Research Center, Nanyang Technological University, 50 Nanyang Avenue, Singapore 630798, Republic of Singapore. Electronic mail: cqxwang@ntu.edu.sg

emational modeling is outlined briefly in Sec. II. The numerical modeling is presented in Sec. III. In Sec. IV, the 3D algorithm is first compared to an experiment and a validated axisymmetric bubble modeling. The numerical analyses are then performed for the evolution of a gas bubble near an inclined wall and the interaction of two gas bubbles and a free surface. Section V summarizes the present work.

II. MATHEMATICAL FORMULATION

Consider the evolution of gas bubbles nearby a rigid wall or beneath a free surface. The fluid in the time-varying domain Ω is assumed to be inviscid, incompressible and the flow irrotational. The velocity potential $\phi(\mathbf{p})$ satisfies the boundary integral equation

$$c(\mathbf{p}) \phi(\mathbf{p}) = \int_{\partial\Omega} \left(\frac{\partial\phi(\mathbf{q})}{\partial n} G(\mathbf{p}, \mathbf{q}) - \phi(\mathbf{q}) \frac{\partial G(\mathbf{p}, \mathbf{q})}{\partial n} \right) dS, \tag{1}$$

where \mathbf{p} is the field point and \mathbf{q} the source point varying as an integration variable on the boundary $\partial\Omega$; $G(\mathbf{p}, \mathbf{q}) = |\mathbf{p} - \mathbf{q}|^{-1}$ is the free space Green function; $c(\mathbf{p})$ is the solid angle under which the fluid domain Ω is viewed from field point \mathbf{p} ; \mathbf{n} is the unit outward normal vector of the fluid domain Ω . The impermeable condition on a plane wall is satisfied by using the image method, and the boundary condition at infinity, $|\nabla\phi| \rightarrow 0$, is satisfied automatically by (1).

The pressure inside a gas bubble consists of the vapor pressure p_c and the pressure of the noncondensing gas following the adiabatic law

$$p_b = p_c + p_0 \left(\frac{V_0}{V} \right)^\lambda, \tag{2}$$

where V_0 and p_0 are the initial volume and pressure of the noncondensable gas, respectively, and λ is the ratio of the specific heats of the gas. We take $\lambda = 1.25$ in this work.

The evolution of the bubble surface and free surface is governed by the kinematic and dynamic boundary conditions, requiring a point on the surfaces to remain on them and the pressure be continuous across them, respectively,

$$\frac{d\mathbf{x}}{dt} = \nabla\phi, \tag{3}$$

$$\frac{d\phi}{dt} = \frac{1}{2} |\nabla\phi|^2 - gz, \quad \text{on a free surface,} \tag{4a}$$

$$\frac{d\phi}{dt} = \frac{p_\infty}{\rho} + \frac{1}{2} |\nabla\phi|^2 - g(z-d) - \frac{1}{\rho} \left(p_c + p_0 \left(\frac{V_0}{V} \right)^\lambda \right), \tag{4b}$$

on a bubble surface,

where g is the gravitational acceleration. The bubble center at its inception is on the plane $z=d$ and p_∞ is the ambient pressure on this plane. The surface tension effects are neglected in (4), which should be included for tiny bubbles at the scale of less than a millimeter.¹¹

We then normalize the variables with respect to length scale R_m (the maximum radius of the bubble) and the pressure scale $\Delta p = p_\infty - p_c$. The normalized dynamics boundary conditions (4) become

$$\frac{d\phi}{dt} = \frac{1}{2} |\nabla\phi|^2 - \delta^2 z, \quad \text{on a free surface,} \tag{5a}$$

$$\frac{d\phi}{dt} = 1 + \frac{1}{2} |\nabla\phi|^2 - \delta^2 (z - \gamma_f) - \varepsilon \left(\frac{V_0}{V} \right)^\lambda, \quad \text{on a bubble surface,} \tag{5b}$$

where $\delta = \sqrt{\rho g R_m / \Delta p}$ is the buoyancy parameter, $\varepsilon = p_0 / \Delta p$ the normalized initial bubble pressure, and $\gamma_f = d / R_m$ the normalized initial depth of the bubble center.

The bubble is assumed to begin its existence at $t=0$ as a high-pressure spherical bubble of radius R_0 with zero radial velocity. The quiescent initial state is given, i.e., $\phi=0$ throughout the entire fluid domain. The initial radius R_0 is solved by the reverse time integration of the Rayleigh equation as follows from the normalized maximum radius of 1.0 to R_0 , referencing Best and Kucera⁴

$$R\ddot{R} + \frac{3}{2} \dot{R}^2 = \varepsilon \left(\frac{R_0}{R} \right)^{3\lambda} - 1. \tag{6}$$

In fact, (6) may be integrated analytically by multiplying through by $2R^2\dot{R}$. Using $\dot{R}=0$ at $R=R_0$ and $R=1$, then a relationship can be obtained between R_0 and ε .⁴

III. NUMERICAL MODELING

The numerical modeling starts with the initial boundary mesh. Following the initial boundary mesh in time provides the boundary mesh at all subsequent time steps. The surface mesh of the initial spherical bubble is based on an icosahedron consisting of 20 equal-sized equilateral triangles and 12 nodes on the sphere surface. This mesh is improved by breaking each of the triangles into smaller equal-sized equilateral triangles and projecting them to the spherical surface. The number of the subdivisions of each of the triangles defines the ‘‘level’’ of the mesh. For the n th level mesh, each original triangle is replaced by n^2 smaller equal-sized triangles. The arbitrary level mesh of a spherical surface has been built using the method.

The initial free surface mesh is obtained by projecting the nodes on the upper half of a meshed sphere surface to a horizontal plane above the sphere. The mesh density and the range of the computational domain of the free surface are controlled by varying the distances of nodes of each ring to the center of the meshed region.

After the boundary mesh, the bubble and free surfaces are represented by means of planar triangular facets with linear distributions of velocity potential ϕ and normal velocity component $\psi = \partial\phi/\partial n$ over each element Δ . The influence coefficients can be expressed as the integrations on each element as follows:

$$A = \int_{\Delta} \frac{\psi(\mathbf{q})}{|\mathbf{p} - \mathbf{q}|} dS = \psi_A A_1 + \psi_B A_2 + \psi_C A_3, \tag{7a}$$

$$B = \int_{\Delta} \phi(\mathbf{q}) \frac{\partial}{\partial n} \left(\frac{1}{|\mathbf{p} - \mathbf{q}|} \right) dS = \phi_A B_1 + \phi_B B_2 + \phi_C B_3, \tag{7b}$$

where

$$A_i = \int_1^0 \int_0^{1-\eta} \frac{f_i(\xi, \eta) J d\xi d\eta}{\sqrt{c_1 \xi^2 + c_2 \eta^2 + c_3 \xi \eta + c_4 \xi + c_5 \eta + c_6}}, \quad (8a)$$

$$B_i = \int_1^0 \int_0^{1-\eta} \frac{f_i(\xi, \eta) \cdot \mathbf{r}_n \cdot J d\xi d\eta}{\sqrt{c_1 \xi^2 + c_2 \eta^2 + c_3 \xi \eta + c_4 \xi + c_5 \eta + c_6}}, \quad (8b)$$

with

$$f_1(\xi, \eta) = \xi, \quad f_2(\xi, \eta) = \eta, \quad f_3(\xi, \eta) = 1 - \xi - \eta, \quad (9a)$$

$$c_1 = |\mathbf{r}_A - \mathbf{r}_B|^2, \quad c_2 = |\mathbf{r}_A - \mathbf{r}_C|^2, \quad (9b)$$

$$c_3 = (\mathbf{r}_A - \mathbf{r}_B) \cdot (\mathbf{r}_A - \mathbf{r}_C), \quad c_4 = (\mathbf{r}_A - \mathbf{r}_B) \cdot (\mathbf{r}_p - \mathbf{r}_A), \quad (9c)$$

$$c_5 = (\mathbf{r}_A - \mathbf{r}_C) \cdot (\mathbf{r}_p - \mathbf{r}_A), \quad c_6 = |\mathbf{r}_p - \mathbf{r}_A|^2, \quad (9c)$$

$$J = |(\mathbf{r}_A - \mathbf{r}_B) \times (\mathbf{r}_A - \mathbf{r}_C)|, \quad (9d)$$

$$\mathbf{r}_n = \mathbf{n} \cdot (\mathbf{r}_p - \mathbf{r}_A).$$

The diagonal elements of the influence coefficient matrixes are integrated analytically. The nondiagonal elements are calculated numerically using 7-, 3- and 1-point Gaussian quadratures for field points at various distances from the element in order to save the CPU time without losing accuracy.

Next, we consider the calculation of the solid angles on the meshed surfaces. For a closed surface, such as a bubble surface, the solid angles are available as a subset of the influence coefficients. The solid angles on the free surface have to be calculated since it is an open surface, which is a tedious task. One can calculate it by adding some artificial surfaces to make it a closed surface, but considerable CPU time is needed since the mesh of the artificial surfaces must be fine to provide a reasonable result. Zhang *et al.*²¹ calculated solid angles numerically involving elliptic functions. Actually, the solid angle can be calculated straightforwardly using the following formula derived from the spherical triangle theory:

$$c(\mathbf{p}) = \sum_{i=1}^{N_b} \delta_i + (2 - N_b) \cdot \pi, \quad (10)$$

where N_b is the number of the surrounding triangles to node \mathbf{p} , and δ_i is the angle between every two connected surrounding triangles.

At last, we proceed to calculate the material velocity on the bubble and free surfaces. A node is a corner of the meshed surfaces and the normal vector at the point is undefined. To calculate the material velocity, the second order polynomial interpolation is implemented for both the surfaces and the potential distributions on them

$$Z = F(X, Y) = a_1 + a_2 X + a_3 Y + a_4 X^2 + a_5 XY + a_6 Y^2. \quad (11)$$

The surfaces may be steep or even parallel to the Z-axis locally, which causes the interpolation to be poor or even singular. Because of this, a local Cartesian coordinate is introduced with its origin at the node considered and its Z-axis in the outward normal direction, which is calculated by averaging the normal vectors of the surrounding elements as

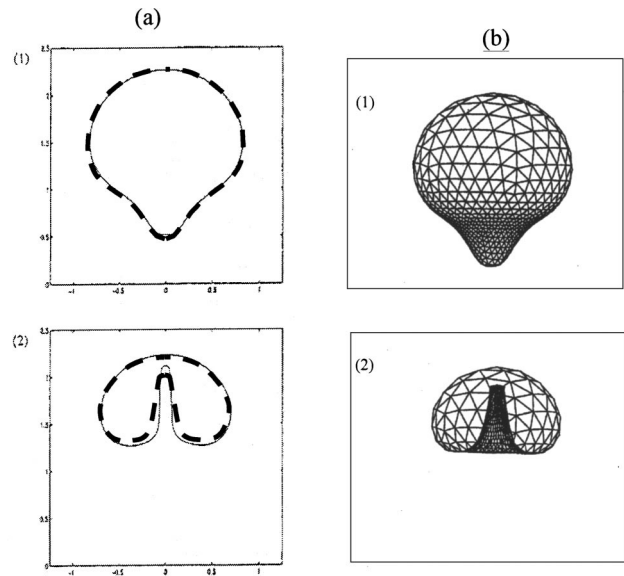


FIG. 1. (a) Comparison of the bubble shapes for a gas bubble above a horizontal wall for $\epsilon = 100$, $\delta = 0.5$, and $\gamma = 1.0$ calculated from the present 3D code (dashed line) and the axisymmetric code (solid line), at dimensionless times: (1) 1.019 and (2) 2.273. (b) The corresponding 3D bubble shapes.

described later on. Zinchenko *et al.*²⁴ and Zhang *et al.*²⁵ made the Z-axis exactly at the normal direction through an iteration method. However, the Z-axis is not necessary to be at the exact normal direction for the interpolation and the iteration method does not improve the accuracy of the interpolation.

The coefficients for the polynomial (11) are determined from the nearest neighboring nodes within $2d$ from the node considered, where d is the mean distance of its surrounding nodes. The coefficients are determined by the weighted least squares method with the error function

$$\sigma(a_1, a_2, a_3, a_4, a_5, a_6) = \sum_{k=1}^N w_k [F(X_k, Y_k) - Z_k]^2, \quad (12)$$

$$N \geq 6,$$

where w_k is the weight function that is determined by the distance of the neighboring node \mathbf{r}_k to node \mathbf{r}_0 considered

$$w_k = \exp\left(-\frac{|\mathbf{r}_k - \mathbf{r}_0|}{2d}\right). \quad (13)$$

The surface normal and tangential velocity at the node considered can then be calculated from the local surface and potential interpolations.

Special attention must be paid for the following situations where the above interpolation scheme is inaccurate or does not work. One situation is where the surface normal change is not small within the mesh size, such as at the bases and fronts of a sharp bubble jet (as shown in Fig. 1) and sharp free surface spike (as shown in Fig. 3). The criterion for the situation is chosen as

$$\text{Max} |\delta_i - \pi| \leq \pi/12, \quad \text{for } i = 1, 2, \dots, N_b, \quad (14)$$

where N_b is the number of the surrounding triangles to node \mathbf{p} , and δ_i is the angle between every two connected surround-

ing triangles to the node considered. Another situation is the neighboring nodes within certain distance (chosen as $2d$ in this work) being less than 6.

Under the above two situations, the outward normal vector of the surface at node r_0 is calculated by averaging the normal vectors of its surrounding elements as follows:

$$n = \frac{\sum_k w_k^c n_k}{\sum_k w_k^c}, \quad \text{with } w_k^c = \exp\left(-\frac{|r_k^c - r_0|}{d_c}\right), \quad (15)$$

where r_k^c is the centers of the surrounding elements, and $d_c = \text{Max}|r_k^c - r_0|$, for $k=1,2,\dots,N_b$. The tangential velocity vector at a node is calculated by averaging the tangential velocity vectors on its surrounding elements in the same way.

At each time step, the normal velocity component on the bubble and free surfaces is calculated with the boundary integral method and the normal vector and tangential velocity vector are calculated with the above hybrid surface interpolation. With the material velocity calculated, the bubble and free surfaces and the velocity potential on them are then updated by integrating (3) and (5) using the predictor-corrector scheme. A variable time step is chosen to ensure the maximum change in the velocity potential being at a small prescribed value, which in this work is chosen as 0.03.

IV. NUMERICAL SIMULATIONS

A. Validations

It has been verified that the algorithm agrees well with the Rayleigh–Plesset solution for a spherical cavitation bubble and converges with mesh sizes and time steps for three-dimensional bubble motion. For brevity we will only describe the comparisons with the axisymmetric code of Wang *et al.*^{12,13} and the experiment of Blake and Gibson.⁹

The first comparison is for a gas bubble with $\varepsilon = 100$ and $\varepsilon = 0.5$ initiated at $\gamma = 1.0$ above a horizontal wall. The bubble shapes are shown in Fig. 1(a) calculated from the 3D code (dashed line) and the axisymmetric code (solid line). The corresponding three-dimensional bubble shapes are depicted in Fig. 1(b) too. The bubble assumes a “strawberry shape” during the early stage of the collapse phase (time sequence 1), and a very sharp upward jet forms at the end of the collapse phase (sequence 2). The results of the two codes are in good agreement, the above features being reproduced by both of them.

The Kelvin impulse of a bubble was introduced by Benjamin and Ellis,²⁶ and was developed by Blake *et al.*^{2,10,27} to derive a criterion governing the directions of the migration and re-entrant jet for bubbles. Our simulations will be compared with the Kelvin impulse theory. The Kelvin impulse is defined as

$$I = \int_{\partial\Omega_b} \phi n dS, \quad (16)$$

where $\partial\Omega_b$ denotes the bubble surface. Best and Blake²⁷ obtained an analytical estimation of the Kelvin impulse of a bubble in the neighborhood of a rigid surface using the Lagally theorem and assuming the bubble to remain spheri-

cal throughout its lifetime. In particular the Kelvin impulse at the end of the collapse phase is given as follows:

$$I = \frac{2\sqrt{6}\pi}{9} \left(B\left(\frac{7}{6}, \frac{3}{2}\right) - \frac{1}{2}\mu B\left(\frac{3}{2}, \frac{3}{2}\right) \right) \Gamma + \frac{4\sqrt{6}\pi}{9} \delta^2 \left(B\left(\frac{11}{6}, \frac{1}{2}\right) + \frac{1}{2}\mu B\left(\frac{13}{6}, \frac{1}{2}\right) \right) k, \quad (17)$$

with an error of $O(1/\gamma^4)$, where μ and Γ are determined by the location and shape of the solid boundary, and $B(x,y)$ is the beta function.²⁸ The first term in (17) results from the effect of the rigid boundary, and the second term in (17) from the effect of buoyancy. For a bubble initiated near an inclined wall, μ and Γ can be calculated as follows:

$$\mu = \frac{1}{2\gamma}, \quad \Gamma = \frac{1}{\gamma^2} (\sin \beta i - \cos \beta k), \quad (18)$$

where i and k are the unit vectors of x - and z -axes, respectively.

Figures 2(a) and 2(b) depict the good agreements of the bubble volume history and Kelvin impulse history calculated

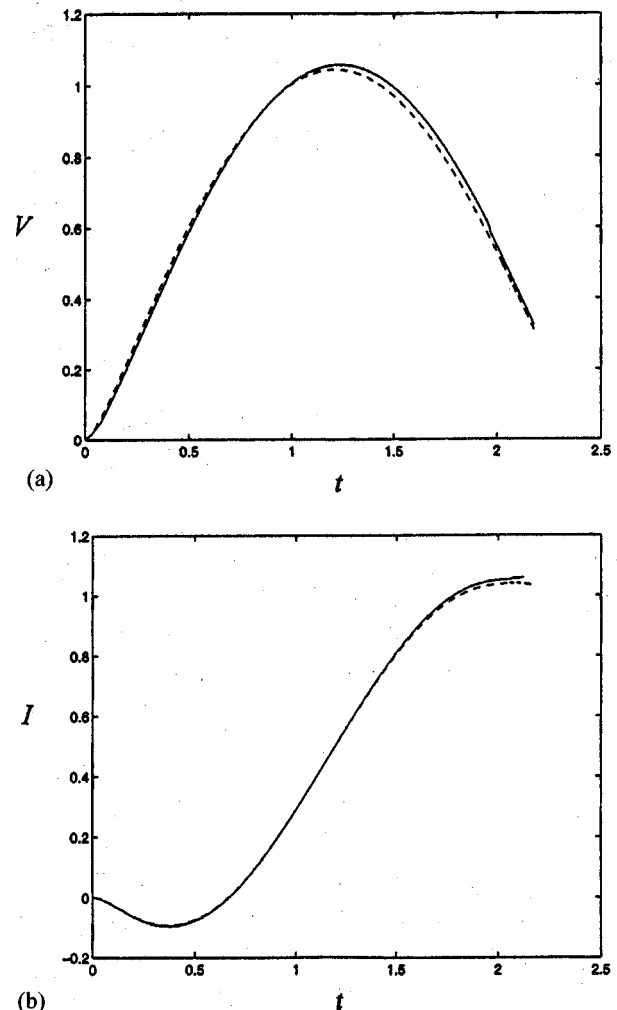


FIG. 2. Comparisons of (a) the volume and (b) the Kelvin impulse versus time for a gas bubble above a wall at $\varepsilon = 100$, $\delta = 0.5$, and $\gamma = 1.0$ calculated from the present 3D code (solid line) and the axisymmetric code (dashed line).

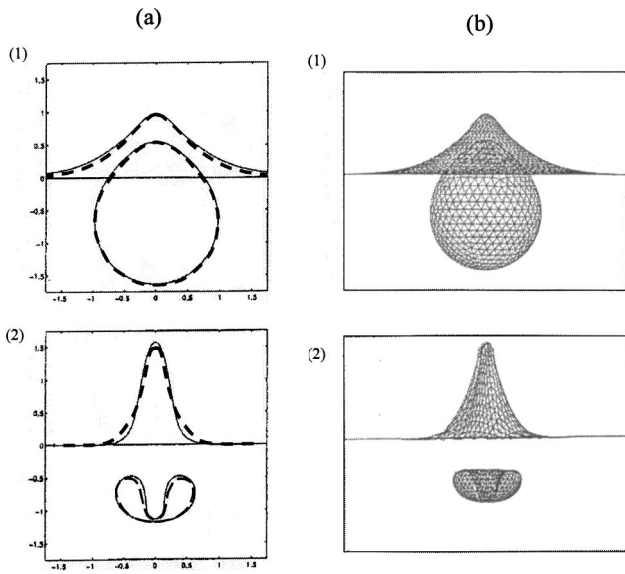


FIG. 3. (a) Comparison of the present 3D code (dashed line) and the axisymmetric code (solid line) of the bubble and free surface shapes for $\epsilon = 100$, $\delta = 0.50$, and $\gamma_f = 0.75$, at dimensionless times: (1) 0.711 and (2) 1.360. (b) The corresponding three-dimensional bubble and free surface shapes.

from the two codes, respectively. At the early stage of the bubble expansion, the effects of the Bjerknes attraction of the wall appear slightly stronger, and the Kelvin impulse decreases with time and is negative, as shown in Fig. 2(b). As the bubble expands, the buoyancy becomes gradually stronger, and the Kelvin impulse increases with time and becomes positive in the middle stage of the expansion phase. It increases quickly as the bubble is around its maximum size, when the buoyancy effect dominates. It does not change significantly at the end of the collapse phase when the two forces seem to be balanced with each other.

The second comparison is for a gas bubble with $\epsilon = 100$ and $\delta = 0.5$ initiated at $\gamma_f = 0.75$ beneath a free surface. The bubble and free surface shapes are shown in Fig.

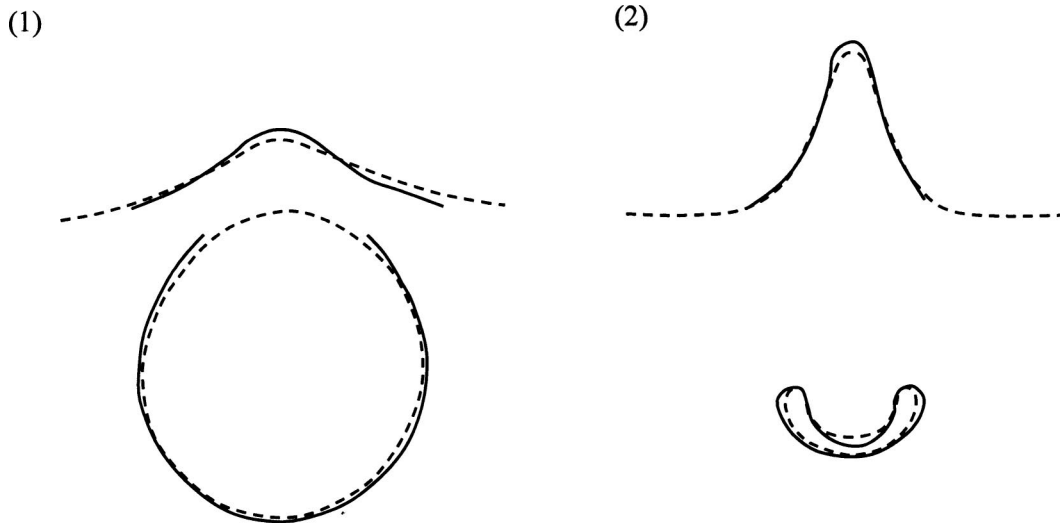


FIG. 4. Comparison of the present 3D code (dashed line) and the experiment of Blake and Gibson (solid line) of the vapor bubble and free surface for $\delta = 0.0$ and $\bar{\gamma}_f = 0.98$, at dimensionless times (1) 0.59 and (2) 1.48 for the simulation, and (1) 0.60 and (2) 1.51 for the experiment.

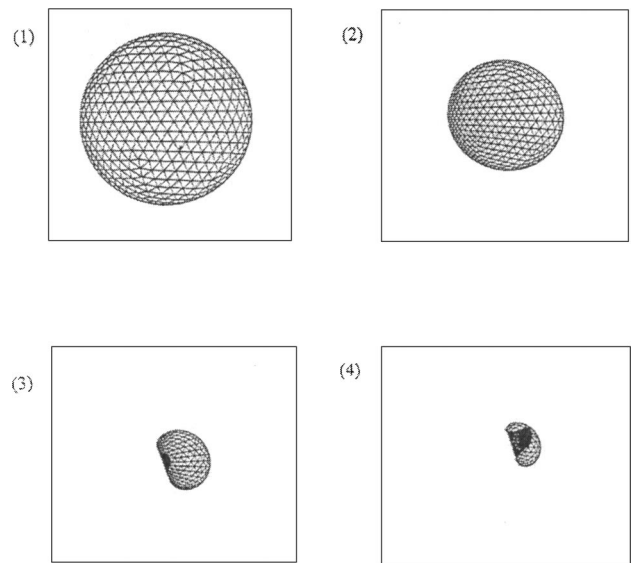


FIG. 5. The evolution of a gas bubble near a vertical wall for $\epsilon = 100$, $\delta = 0.5$, and $\gamma = 3.0$, at dimensionless times (1) 1.274, (2) 1.979, (3) 2.082, and (4) 2.123.

3(a) calculated from the 3D code (in dashed line) and axisymmetric code (solid line), together with the corresponding three-dimensional shapes in Fig. 3(b). At the end of the expansion phase (sequence 1), the top part of the bubble surface enters into the base of the free surface causing a substantial free surface hump. At the end of the collapse phase (sequence 2), a downward bubble jet forms, and a sharp spike forms on the free surface. Once again the results of the two codes agree well, all the above features being reproduced. The bubble jet in Fig. 1 and free surface spike in Fig. 3 calculated from the 3D code are not as sharp as the axisymmetric results, which could be due to the coarser mesh used in the three dimensional simulations.

The third comparison is against to the experiment of Blake and Gibson⁹ for a vapor bubble with $\delta = 0.0$ initiated

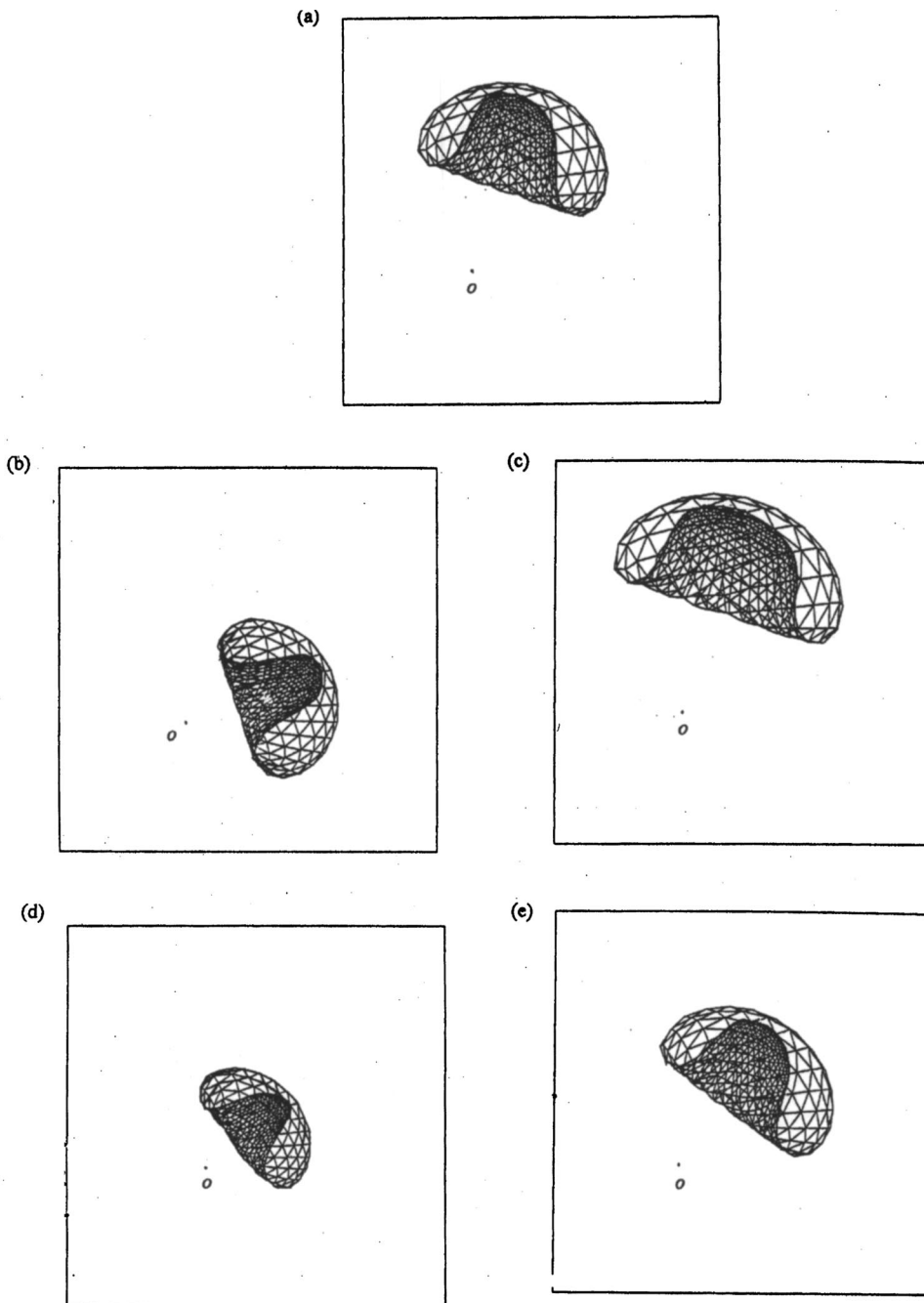


FIG. 6. The shapes of a gas bubble near a wall at the end of the collapse phase characterized by $\varepsilon=100$, $\gamma=3.0$ and (a) $\delta=0.1473$, $\beta=\pi/2$; (b) $\delta=0.074$, $\beta=\pi/2$; (c) $\delta=0.221$, $\beta=\pi/2$; (d) $\delta=0.147$, $\beta=\pi/4$; and (e) $\delta=0.1473$, $\beta=3\pi/4$, respectively.

at $\bar{\gamma}_f=0.98$ beneath a free surface. $\bar{\gamma}_f$ is the initial depth of the bubble normalized by a half of its maximum horizontal width, which is the length scale deployed in the experiment. The initial boundary condition for the vapor bubble is assumed as $\phi(t_0)=-2.58$ at $t_0=0.001553$ and $R_0=0.1$. Figure 4 shows the shapes of the bubble and free surface of the experiment (in solid line) and the computation (dashed line). The evolution of the bubble and free surface of this case is similar to that of the above case, except a broad jet forms and the bubble assumes a “bowl shape” at the end of the collapse phase [Fig. 4(b)]. The simulation and experiment agree well generally. There are small differences in the timings of the events and the detailed free surface and bubble shapes, which could be due to the computation resolution, the measurement

accuracy, the matching of the initial conditions, as well as the viscous effects and/or surface tension neglected in the computation.

B. A bubble near an inclined wall

Having validated the 3D bubble code, we proceed to investigate the evolution of a gas bubble initiated near an inclined wall. The first case considered is for a gas bubble with $\varepsilon=100$ and $\delta=0.1473$ initiated at $\gamma=3.0$ from a vertical wall. Figure 5 depicts the collapse of the bubble, since it is nearly spherical during the expansion phase. It is still close to a spherical shape for most of the collapse phase. Only at the end of the collapse phase, the bubble becomes a kidney

TABLE I. The comparison of the angles of the reentrant jets to the horizontal plane for a gas bubble with $\varepsilon = 100$ initiated at $\gamma = 3.0$ from an inclined wall calculated from the 3D bubble code and Kelvin impulse theory.

Cases	$\delta = 0.1473,$ $\beta = \pi/2$	$\delta = 0.074,$ $\beta = \pi/2$	$\delta = 0.221,$ $\beta = \pi/2$	$\delta = 0.1473$ $\beta = \pi/4$	$\delta = 0.1473,$ $\beta = 3\pi/4$
3D bubble code	52°	17°	70°	36°	70°
Kelvin impulse theory	49°	16°	69°	32°	69°

shape, and a re-entrant jet forms in a very short period. The bubble remains approximately a spherical shape for more than 90% of its lifetime and the jetting time (from the start of the jet to its impact on the opposite bubble wall) occupies only about 2% of its lifetime. The buoyancy and Bjerknes attraction of the wall are close to each other in magnitude for this case as $\gamma\delta = 0.442$; consequently, the jet is roughly in their bisection as predicted by the Kelvin impulse theory.^{2,27}

To investigate the buoyancy effects, the above case is recalculated at $\delta = 0.074$ ($\gamma\delta = 0.442/2$) and $\delta = 0.221$ ($\gamma\delta = 0.442 \times 1.5$), a weak buoyancy case and a strong one, respectively. The effects of the wall inclination are investigated by recalculating the case at $\beta = \pi/4$ and $3\pi/4$, respectively, where β is the inclined angle of the wall to the x -axis. The evolution patterns of those four cases are very similar to that of the first case as shown in Fig. 5, except the bubble shapes and jet directions at the end of the collapse phase are different as shown in Fig. 6. The bubble shapes and jet directions are roughly symmetrical in the jet direction. To provide the rough direction of the bubble migration, its center "o" at the inception is also drawn in the figure for each of the cases. One can see the jet direction roughly coincides with that of the motion of the bubble center.

The jet angles to the horizontal plane are measured from Fig. 6 and listed in Table I. The jet angles are also calculated using the Kelvin impulse theory referencing Blake *et al.*,²⁷ which are listed in Table I for comparison. The jet directions

calculated from the 3D bubble code agree well with those of the Kelvin impulse theory for all the above 5 cases with a maximum difference of 4°.

Next, we consider the bubble initiated closer to the wall. Figure 7 depicts the collapse of the bubble with $\varepsilon = 100$ and $\delta = 0.221$ initiated at $\gamma = 2.0$ from a vertical wall. Its collapse pattern is similar to that of the cases at $\gamma = 3.0$, remaining spherical for most of its lifetime and a re-entrant jet forming in a short period at the end of the collapse phase. The buoyancy should be close to the Bjerknes attraction of the wall for the case as $\gamma\delta = 0.442$, but the jet is asymmetric and roughly in upwards direction, rather than in the bisection of the two forces.

Figure 8 depicts the evolution of the bubble at $\varepsilon = 100$ and $\delta = 0.5$ initiated at $\gamma = 1.0$ below an inclined wall at β

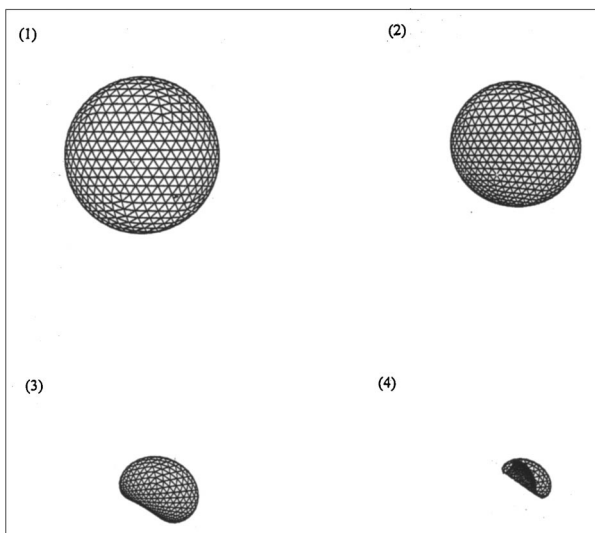


FIG. 7. The evolution of a gas bubble near a vertical wall for $\varepsilon = 100$, $\delta = 0.221$, and $\gamma = 2.0$, at dimensionless times: (1) 1.058, (2) 1.995, (3) 2.093, and (4) 2.178.

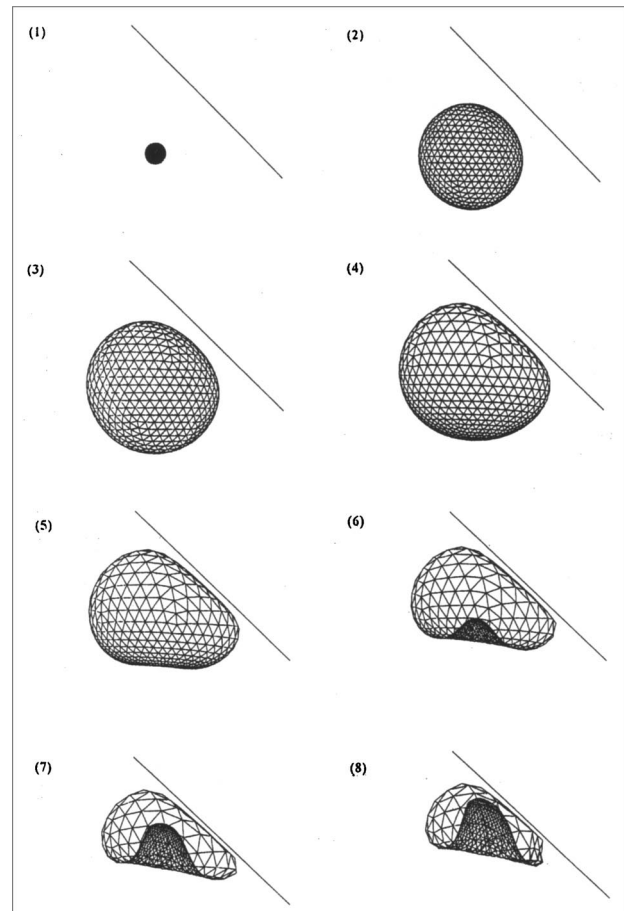


FIG. 8. The evolution of a gas bubble near a wall for $\varepsilon = 100$, $\delta = 0.5$, $\gamma = 1.0$, and $\beta = 3\pi/4$, at dimensionless times: (1) 0.000, (2) 0.313, (3) 0.651, (4) 1.317, (5) 1.598, (6) 1.878, (7) 2.092, and (8) 2.195.

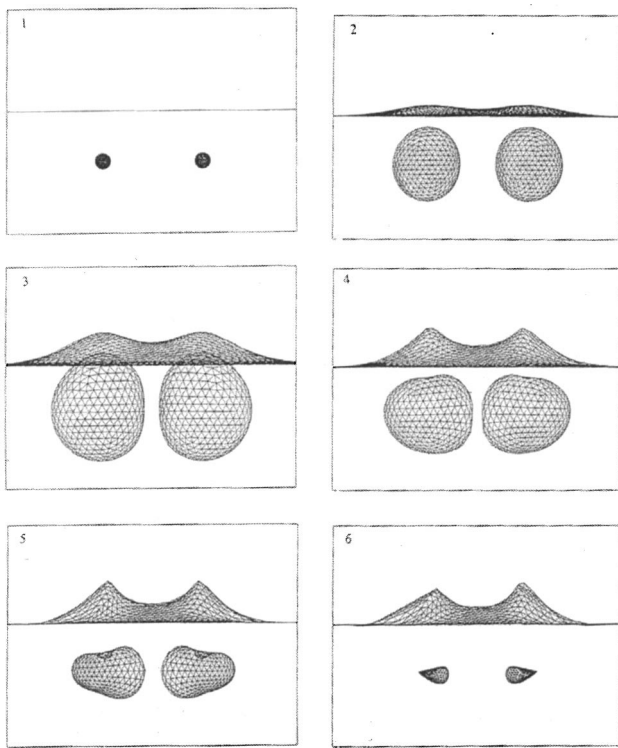


FIG. 9. The evolution of two gas bubbles beneath a free surface for $\varepsilon = 100$, $\delta = 0.5$ initiated at $\gamma_f = 1.0$, at dimensionless times: (1) 0.000, (2) 0.236, (3) 1.030, (4) 1.240, (5) 1.450, and (6) 1.562.

$= 3\pi/4$, it expands spherically except for a large part of the bubble surface near the wall having been oppressed by the wall since the middle stage of the expansion phase (sequences 1–4). An upward jet inclined slightly to the wall forms since the middle stage of the collapse phase (sequences 6–8), which will impact upon the rigid wall as soon as it penetrates the bubble. The algorithm stands well when a large part of the bubble surface has been very close to the wall for the whole collapse phase (sequences 4–8), with the gap between them being less than the element size.

C. Two bubbles beneath a free surface

In this section, we address the interaction of two gas bubbles and a free surface nearby. The two gas bubbles are chosen at $\varepsilon = 100$ and $\delta = 0.5$, and the normalized horizontal distance between their centers at their inception being 2.0. Figure 9 shows the interaction of the two bubbles at $\gamma_f = 1.0$, which are equivalent to a bubble near a free surface and a rigid wall at the symmetry. The bubble is under the influence of buoyancy, the Bjerknes repellent from the free surface, and the Bjerknes attraction from the symmetry wall, which should be comparable in magnitude in this case according to the Kelvin impulse theory. At the end of the expansion phase (sequence 3), the surface of each of the two bubbles near the symmetry wall are attracted and flattened by the other one. The upper parts of the bubble surfaces become elongated and enter into the base of the raised free surface producing two free surface humps above them. As the bubbles collapse, each of them is influenced by the upward buoyancy and downward Bjerknes repellent of the free sur-

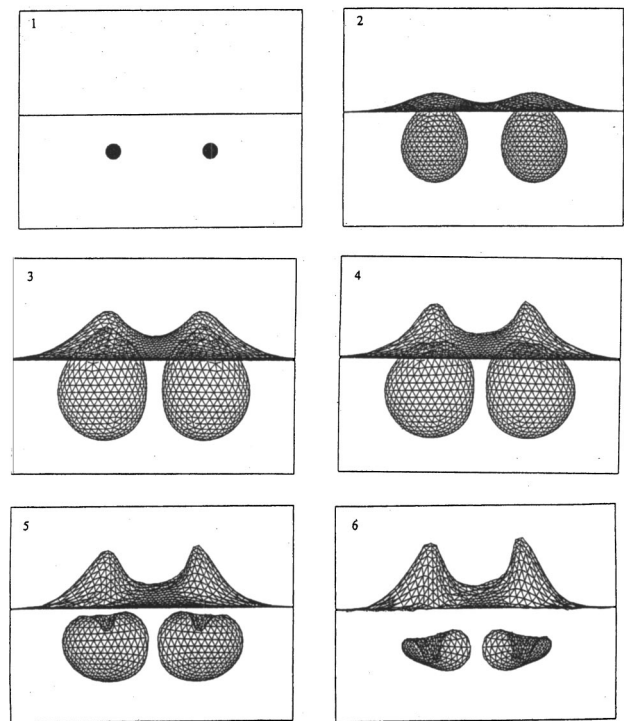


FIG. 10. The evolution of two gas bubbles beneath a free surface for $\varepsilon = 100$ and $\delta = 0.5$ initiated at $\gamma_f = 0.75$, at dimensionless times: (1) 0.000, (2) 0.236, (3) 0.716, (4) 0.939, (5) 1.144, and (6) 1.402.

face and attracted by the other one. As the result, the bubbles assume oblate shapes with larger parts near to the symmetry wall (sequence 5), and triangle shapes in the view plane at the end of the collapse phase (sequence 6). As the bubbles collapse, the parts of the free surface above them roughly remain their heights and the rest of the free surface falls (sequences 4–6).

The second case is for the two bubbles initiated at $\gamma_f = 0.75$, being nearer to the free surface as shown in Fig. 10. At the end of the expansion phase, much more of the bubble surfaces enter into the base of the raised free surface producing higher free surface humps above them (sequence 3). As the bubbles collapse (sequences 4–6), the tops of the two bubbles move down forming two large downward jets due to the stronger repulsion by the free surface. The two jets are inclined to the symmetry wall due to the attraction between the two bubbles. In the meantime, only the parts of the free surface above the bubbles rise continuously and the rest of the free surface falls, resulting in two free surface spikes (sequences 4–6).

Comparing a single bubble near a free surface at the same parameters (Fig. 3), the maximum height of the free surface spikes of the two-bubble case is lower. The mechanism underlying the phenomenon can be explained as follows. As the bubbles collapse, the fluid is drawn rapidly into the regions between the free surface and the bubbles. For the axisymmetric case, a stagnation point is formed along the axis of symmetry with a high-pressure region over there, which redirects the incoming flow from the sides downward to form the downward bubble jet and upwards to form the

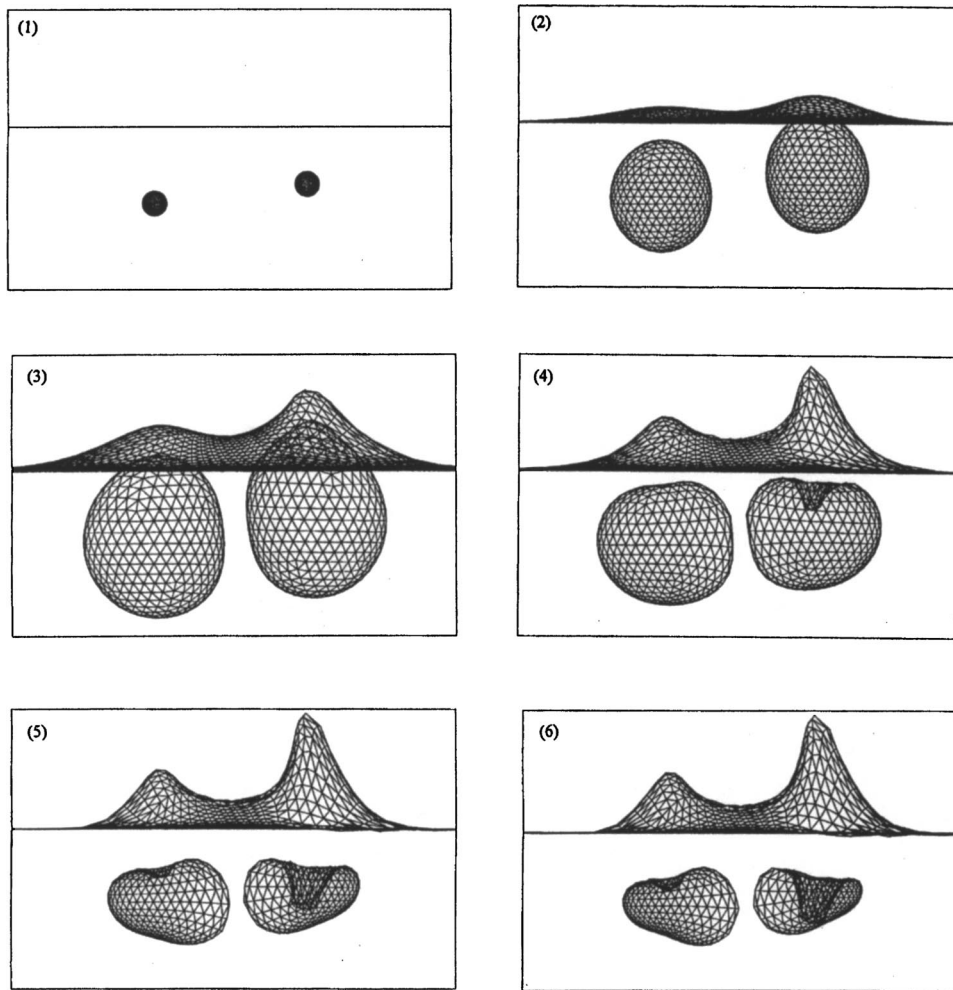


FIG. 11. The evolution of two gas bubbles beneath a free surface for $\varepsilon = 100$ and $\delta = 0.5$ initiated at $\gamma_f = 0.75$ and 1.0 , respectively, at dimensionless times: (1) 0.000, (2) 0.223, (3) 0.463, (4) 0.734, (5) 1.368, and (6) 1.411.

free-surface spike simultaneously. For the two-bubble case, less fluid from the symmetry wall side is drawn into the region as compared to the open side; consequently, the high-pressure region formed is not as strong as the axisymmetric case, and the corresponding free surface spikes and bubble jets are weaker.

The last case is for the two gas bubbles initiated at $\gamma_f = 1.0$ and 0.75 , respectively (Fig. 11). The evolution of the bubble and the free surface at each side is similarly to that of the two bubbles initiated at the corresponding depth as shown in Figs. 9 and 10, respectively. The jet forms early on the bubble initiated nearer to the free surface and it has impacted the opposite bubble wall at the end of the simulation (sequence 6), when the other bubble is still collapsing. This is as expected since the bubble lifetime decreases with its initial depth.^{12,13} The free surface spike above the bubble at $\gamma_f = 0.75$ in this case is higher than that of the two bubbles initiated at the depth.

V. SUMMARIES

A robust mixed-Eulerian–Lagrangian modeling is described to simulate the violent bubble motion by implementing a hybrid surface interpolation for calculating the material velocity at the bubble and free surfaces. A linear averaging approximation is deployed for the parts of the surfaces where

the change of the surface normal vector within the element size is not small, such as the bases and fronts of the re-entrant jet and free surface spike. A polynomial scheme coupled with the weighted moving least squares method is deployed for all other places. The solid angles on the free surface (an open surface) are computed analytically in a closed form. The algorithm is validated against the experiment of Blake and Gibson⁹ and an axisymmetric bubble code.^{12,13} Using this method, we investigate (i) the evolution of a gas bubble near an inclined wall, and (ii) the interaction of two gas bubbles and a nearby free surface. The bubble evolution is followed until the re-entrant jet impacts on the opposite bubble surface (within the element size) without numerical instabilities occurring.

When a gas bubble initiated at $3.0R_m$ or more from an inclined wall, the bubble remains spherical for most of its lifetime. It becomes a kidney shape at the end of the collapse phase and a high-speed liquid jet forms around 2% of the bubble lifetime. The jet is roughly symmetrical and its direction can be predicted approximately by the Kelvin impulse theory.²⁷ For a bubble initiated within $2.0R_m$ from an inclined wall, the re-entrant jet is not symmetrical. The jet is in upwards as the buoyancy and the Bjerknes attraction of the wall being comparable rather than in the bisection of the two forces as predicted by the Kelvin impulse theory.

When two bubbles initiated nearby a free surface, one bubble being attracted by another, but the bubble jet direction largely depends on magnitudes of the forces associated with the buoyancy and repulsion from the free surface. For two gas bubbles at $\delta=0.5$, initial depth $1.0R_m$ and initial distance $2.0R_m$ between them, the three forces should be close in magnitude according to the Kelvin impulse theory. The upward buoyancy and downward repellent of the free surface are balanced; nevertheless, the attraction of the symmetry wall does not produce any jet as expected. The free surface motion above each of the bubbles is not affected significantly by the other one. The free surface rises as two bubbles expanding; when their initial depths are less than $1.0R_m$, the parts of the free surface above the bubbles rise continuously and the rest of the free surface falls as they collapse. As the result, two spectacular free surface spikes form above the two bubbles, with their heights being slightly lower than a single bubble case.

ACKNOWLEDGMENTS

The author wants to express his sincere thanks to the referees of this paper for their valuable suggestions. He also wants to express his sincere thanks to E. K. Png and Dr. Y. W. Chan at DSO National Laboratories for their valuable help and support to this work.

- ¹L. Guerri, G. Lucca, and A. Prosperetti, "A numerical method for the dynamics of nonspherical cavitation bubbles," in Proceedings of the 2nd International Colloquium on Drops and Bubbles, California, 1981, p. 175.
- ²J. R. Blake, B. B. Taib, and G. Doherty, "Transient cavities near boundaries. Part 1. Rigid boundary," *J. Fluid Mech.* **170**, 479 (1986).
- ³G. R. Baker and D. W. A. Moore, "The rise and distortion of a two-dimensional gas bubble in an inviscid liquid," *Phys. Fluids A* **1**, 1451 (1989).
- ⁴J. P. Best and A. Kucera, "A numerical investigation of non-spherical rebounding bubbles," *J. Fluid Mech.* **245**, 137 (1992).
- ⁵S. Zhang and J. H. Duncan, "On the nonspherical collapse and rebound of a cavitation bubble," *Phys. Fluids* **6**, 2352 (1994).
- ⁶H. Yuan and A. Prosperetti, "Gas-liquid heat transfer in a bubble collapsing near a wall," *Phys. Fluids* **9**, 127 (1997).
- ⁷E. A. Brujan, G. S. Keen, A. Vogel, and J. R. Blake, "The final stage of the collapse of a cavitation bubble close to a rigid boundary," *Phys. Fluids* **14**, 85 (2002).
- ⁸K. M. DeBisschop, M. J. Miksis, and D. M. Eckmann, "Bubble rising in an inclined channel," *Phys. Fluids* **14**, 93 (2002).
- ⁹J. R. Blake and D. C. Gibson, "Growth and collapse of a vapor cavity near a free surface," *J. Fluid Mech.* **111**, 123 (1981).

- ¹⁰J. R. Blake, B. B. Taib, and G. Doherty, "Transient cavities near boundaries. Part 2. Free surface," *J. Fluid Mech.* **181**, 197 (1987).
- ¹¹J. R. Blake, J. M. Boulton-Stone, P. B. Robinson, and P. R. Tong, "Collapsing cavities, toroidal bubbles and jet impact," *Philos. Trans. R. Soc. London, Ser. A* **355**, 537 (1997).
- ¹²Q. X. Wang, K. S. Yeo, B. C. Khoo, and K. Y. Lam, "Nonlinear interaction between gas bubble and free surface," *Comput. Fluids* **25**, 607 (1996).
- ¹³Q. X. Wang, K. S. Yeo, B. C. Khoo, and K. Y. Lam, "Strong interaction between buoyancy bubble and free surface," *Theor. Comput. Fluid Dyn.* **8**, 73 (1996).
- ¹⁴G. L. Chahine and T. O. Perdue, "Simulation of the three-dimensional behavior of an unsteady large bubble near a structure," in *Drops and Bubbles, Third International Colloquium*, Monterey, CA, edited by T. G. Wang (American Institute of Physics, New York, 1988), pp. 188-199.
- ¹⁵G. L. Chahine, "Numerical modeling of the dynamic behavior of bubble in nonuniform flow field," in ASME Symposium on Numerical Methods for Multiphase Flows, Toronto, 1990.
- ¹⁶S. A. Wilkerson, "A boundary integral approach to three-dimensional underwater explosion bubble dynamics," Ph.D. dissertation, Johns Hopkins University, Baltimore, MD, 1990.
- ¹⁷P. J. Harris, "A numerical model for determining the motion of a bubble close to a fixed rigid structure in a fluid," *Int. J. Numer. Methods Eng.* **33**, 1813 (1992).
- ¹⁸P. J. Harris, "A numerical method for predicting the motion of a bubble close to a moving rigid structure," *Commun. Numer. Methods Eng.* **9**, 81 (1993).
- ¹⁹L. Chen, J. A. Reizes, and E. Leonardi, "A numerical study of bubble motion in a gravitational field," in 12th Australian Fluid Mechanics Conference, The University of Sydney, 1995, Vol. 2, p. 827.
- ²⁰J. R. Blake, J. M. Boulton-Stone, and P. R. Tong, "Boundary integral methods for rising, bursting and collapsing bubbles," in *BE Applications in Fluid Mechanics*, edited by H. Power (Computational Mechanics, Southampton, UK, 1995), Vol. 4, p. 31.
- ²¹Y. L. Zhang, K. S. Yeo, B. C. Khoo, and W. K. Chong, "Three-dimensional computation of bubbles near a free surface," *J. Comput. Phys.* **146**, 105 (1998).
- ²²M. S. Plesset and A. Prosperetti, "Bubble dynamics and cavitation," *Annu. Rev. Fluid Mech.* **9**, 145 (1977).
- ²³J. R. Blake and D. C. Gibson, "Cavitation bubbles near boundaries," *Annu. Rev. Fluid Mech.* **19**, 99 (1987).
- ²⁴A. Z. Zinchenko, M. A. Rother, and R. H. Davis, "A novel boundary-integral algorithm for viscous interaction of deformable drops," *Phys. Fluids* **9**, 1493 (1997).
- ²⁵Y. L. Zhang, K. S. Yeo, B. C. Khoo, and C. Wang, "3D jet impact and toroidal bubbles," *J. Comput. Phys.* **166**, 336 (2001).
- ²⁶T. B. Benjamin and A. T. Ellis, "The collapse of cavitation bubbles and pressure thereby produced against solid boundary," *Philos. Trans. R. Soc. London, Ser. A* **260**, 221 (1966).
- ²⁷J. P. Best and J. R. Blake, "An estimate of the Kelvin impulse of a transient cavity," *J. Fluid Mech.* **261**, 75 (1994).
- ²⁸M. Abramowitz and I. A. Stegun, *Handbook of Mathematical Functions* (Dover, New York, 1965).